

Non-linear instability analysis of the two-dimensional Navier-Stokes equation: The Taylor-Green vortex problem

Cite as: Phys. Fluids **30**, 054105 (2018); <https://doi.org/10.1063/1.5024765>

Submitted: 04 February 2018 • Accepted: 01 May 2018 • Published Online: 21 May 2018

 Tapan K. Sengupta, Nidhi Sharma and  Aditi Sengupta

COLLECTIONS

 This paper was selected as an Editor's Pick



View Online



Export Citation



CrossMark

ARTICLES YOU MAY BE INTERESTED IN

[Vorticity dynamics of the three-dimensional Taylor-Green vortex problem](#)

Physics of Fluids **31**, 035106 (2019); <https://doi.org/10.1063/1.5083870>

[Non-linear instability analysis of the three-dimensional Navier-Stokes equations: Taylor-Green vortex problem](#)

Physics of Fluids **32**, 064102 (2020); <https://doi.org/10.1063/5.0006683>

[Clustering of inertial spheres in evolving Taylor-Green vortex flow](#)

Physics of Fluids **32**, 043306 (2020); <https://doi.org/10.1063/5.0002406>

APL Machine Learning

Open, quality research for the networking communities

Now Open for Submissions

LEARN MORE

AIP
Publishing

Non-linear instability analysis of the two-dimensional Navier-Stokes equation: The Taylor-Green vortex problem

Tapan K. Sengupta,^{1,a)} Nidhi Sharma,¹ and Aditi Sengupta²

¹HPCL, Department of Aerospace Engineering, IIT Kanpur, Kanpur, UP, India

²Department of Engineering, University of Cambridge, Cambridge, United Kingdom

(Received 4 February 2018; accepted 1 May 2018; published online 21 May 2018)

An enstrophy-based non-linear instability analysis of the Navier-Stokes equation for two-dimensional (2D) flows is presented here, using the Taylor-Green vortex (TGV) problem as an example. This problem admits a time-dependent analytical solution as the base flow, whose instability is traced here. The numerical study of the evolution of the Taylor-Green vortices shows that the flow becomes turbulent, but an explanation for this transition has not been advanced so far. The deviation of the numerical solution from the analytical solution is studied here using a high accuracy compact scheme on a non-uniform grid (NUC6), with the fourth-order Runge-Kutta method. The stream function-vorticity (ψ, ω) formulation of the governing equations is solved here in a periodic square domain with four vortices at $t = 0$. Simulations performed at different Reynolds numbers reveal that numerical errors in computations induce a breakdown of symmetry and simultaneous fragmentation of vortices. It is shown that the actual physical instability is triggered by the growth of disturbances and is explained by the evolution of disturbance mechanical energy and enstrophy. The disturbance evolution equations have been traced by looking at (a) disturbance mechanical energy of the Navier-Stokes equation, as described in the work of Sengupta *et al.*, “Vortex-induced instability of an incompressible wall-bounded shear layer,” *J. Fluid Mech.* **493**, 277–286 (2003), and (b) the creation of rotationality via the enstrophy transport equation in the work of Sengupta *et al.*, “Diffusion in inhomogeneous flows: Unique equilibrium state in an internal flow,” *Comput. Fluids* **88**, 440–451 (2013). *Published by AIP Publishing.* <https://doi.org/10.1063/1.5024765>

I. INTRODUCTION

Evolution of the Taylor-Green vortices is a benchmark problem of fluid dynamics, originally solved by Taylor and Green¹ by a perturbation series in time, to explain the creation of small scales by vortex stretching, apart from convection and diffusion in a three-dimensional (3D) flow field. The analysis was extended by Goldstein² by a perturbation method, wherein the series was formed as a function of Reynolds number (Re). However, both these finite term linear perturbation methods develop singularities in time and Re , respectively. This breakdown of series solution^{1,2} has been stated to cause instability for the creation of turbulence.

Here we note that there is an analytical solution which is periodic in all spatial dimensions and time-dependent. Thus, the analytical solution can be identified as a time-dependent base flow state, whose instability has not been reported so far by linear or non-linear mechanisms. Gau and Hattori³ have tried to study the modal and non-modal stability of 2D Taylor-Green vortices. However, in the study, *the base flow is assumed to be steady* as their calculated solution is limited only up to $t_{max} = 15$. It is essential to note that in their notations, the Reynolds number is defined in terms of the time-dependent amplitude of the analytic solution for the stream function and hence a longer time solution would make the Reynolds number also time varying. In the present research, no such restrictive

assumption is made. Also the nonlinear study employed does not require finite amplitude excitation. The main aim is to show that the ensuing instability is triggered by background numerical error. For this reason, simulations have been performed using multiple grids to minimize the possibility of truncation errors playing any major role, although these results are not shown here. The use of a compact scheme with its near-spectral accuracy⁴ brings down the truncation error significantly, and the round off error is enough to trigger the nonlinear instability.

There are other differences between the present nonlinear approach and the linear approach,³ one of the primary ones being that the vortices considered are elliptic in shape, while the present study considers circular vortices and the boundary conditions are strictly periodic. In the work of Gau and Hattori,³ there are two types of boundary conditions considered: the penetrating and non-penetrating types to introduce zero normal velocity components on the dividing surface between neighbouring cells for the latter. This non-penetrating type boundary condition isolates each cell, while for the penetrating case the neighbouring cells interact. While this approach may divide the disturbances by their symmetries, the basic periodicity of the Taylor-Green vortices is not strictly enforced. The present approach of considering multiple cells with periodic boundary conditions allows one to study the natural dynamics of the system by including the saddle point (hyperbolic stagnation point³) in the interior of the domain, and its dynamics is governed by

^{a)}Electronic mail: tkxen@iitk.ac.in

the Navier-Stokes equation and not restricted by imposed boundary conditions.

A 3D analytical solution at $t = 0$ has been used by Orszag,⁵ to demonstrate numerically how 3D flow develops. The numerical solution computed by the pseudo-spectral direct numerical simulation (DNS), and the Adams-Bashforth scheme for time integration, has been reported.⁵ However, the critique of this method^{4,6,7} is important due to the role of the spurious mode in three-time level methods. It has been shown recently that pseudo-spectral methods, with Adams-Bashforth time discretization, display the focusing phenomenon when computations are continued for a long time.⁷

Results by Orszag⁵ display the instability numerically, which leads to the typical energy spectrum and dissipation of 3D turbulent flows. This has also been reported in the studies of Brachet⁸ and Brachet *et al.*,^{9,10} considering both inviscid and viscous dynamics of TGV.

Since the appearance of the work by Orszag,⁵ the TGV problem has been used to validate and compare performances of numerical schemes, while developing methods for DNS and large eddy simulation (LES). However, the numerical solution of the TGV flow is not stable with respect to omnipresent background disturbances. A finite difference *wave resolving LES* code, using the explicit spatial discretization and Runge-Kutta time integration method, has been used to test a compressible code for simulating the TGV problem.¹¹ The conventional LES and monotone integrated LES (MILES) were assessed¹² in simulating *the dynamics of transition to turbulence in the TGV flow*. Various subgrid scale (SGS) model results were compared with the MILES solution, where the latter provided accurate estimates of kinetic energy dissipation, energy spectra, enstrophy, and kinetic energy decay.¹² The consequences of filtering 3D numerical results of *nearly incompressible, inviscid TGV flow*, using a spectral method and another fifth-order weighted essentially non-oscillatory method, were investigated in the work of Shu *et al.*¹³ A comparison of a hybrid particle-mesh vortex method with a pseudo-spectral method has been presented by van Rees *et al.*¹⁴ for the TGV flow at $Re = 1600$. Gassner and Beck¹⁵ compared a very high order discontinuous Galerkin (DG) approximation and a low-order discretization for solving the TGV problem to prove the superiority of higher order methods. The analytical solution of the TGV flow offers an advantage of accurate representation in DG approximation, and Chapelier *et al.*¹⁶ used the modal DG method in predicting the TGV flow features by DNS and LES.

A 2D study has been reported in Brachet *et al.*¹⁷ for the dynamics of freely decaying turbulence using the TGV flow as a spatially periodic model problem. However, turbulence was initiated by using initial conditions given by Gaussian-random data, i.e., not using the initial condition used by Taylor and Green.¹ It was found that the inertial energy-spectrum exponent changes from $-4(k^{-4})$ to $-3(k^{-3})$ with evolution of time. The first regime was associated with isolated vorticity-gradient sheets (as predicted by Ref. 18), whereas the second regime (a statistical state) relates to an enstrophy cascade proposed by Kraichnan¹⁹ and Batchelor.²⁰ The small-scales of 2D turbulence are explained as due to stretching of vorticity gradients.

2D DNS of the Navier-Stokes equation for flow over a flat plate caused by wall and free-stream excitations has shown the presence of k^{-3} energy spectrum in the inertial subrange.²¹ It is interesting to note that Nastrom *et al.*²² compiled atmospheric data to show the simultaneous presence of the k^{-3} and $k^{-5/3}$ spectrum for velocity components and potential temperature. However, it is noted²¹ that the k^{-3} part of the spectrum dominates with 98.3% of the area under the curve plotted for spectral density versus k , for the components of velocity and potential temperature.²² The 2D TGV problem allows one to study the evolution of the disturbance field, viewed as a departure of the computed solutions from the analytical laminar solution.

Here, the 2D TGV problem is desirable from physical and numerical point of views for the following reasons: (i) one can take a larger number of grid points compared to a 3D problem, due to which truncation error and other sources of errors like additional aliasing error from vortex stretching term are reduced, and (ii) one can use the analytical solution of the TGV problem from the Navier-Stokes equation as the equilibrium solution. This also forms a basis to judge the quality of numerical methods by comparing solutions at early times, before the onset of physical instability. We use a sixth order compact scheme^{23,24} developed for non-uniform grids in the physical plane to achieve higher resolution, which is not possible with Fourier spectral methods requiring a uniform grid.^{5,8,9}

For any high accuracy computing, uncertainty quantification connotes characterization of error and its propagation. The ubiquitous error in any numerical simulation has to be minimized. Many efforts in analyzing error dynamics have used various methods attributed to von Neumann analysis,^{25,26} which uses an intuitive observation that for a linear system, the error and the signal follow the same dynamics. This has been in use for linear equations and quasi-linearized form of non-linear equations. The error analysis performed with Fourier series cannot explain many situations, which prompted Zingg²⁷ to note that *through Fourier analysis, one can evaluate the phase and amplitude error of a given method as a function of the wavenumber. However, this information can be difficult to interpret*. This epistemic aberration was rectified by developing global spectral analysis (GSA) with the help of the model 1D convection equation.²⁸ One of the striking features of GSA is that the constant phase speed of the convection equation becomes dependent on the wavenumber in numerical simulations. The same feature of the constant coefficient of diffusion changing with wavenumber numerically has been established for the 1D diffusion equation.²⁹ Two other striking successes of GSA are in explaining the spurious upstream propagating q -waves and the phenomenon of focusing of error.⁷ These are with respect to the linear 1D wave equation. The non-linear error dynamics of the KdV equation have also been reported.³⁰ The error dynamics from the numerical solution of the Navier-Stokes equation have yet to be attempted. Thus, the present research utilizes the time-dependent base flow of the Navier-Stokes equation to study its error dynamics and how it triggers the physical instability. This enables us to study the error dynamics of the full Navier-Stokes equation for a time-dependent dynamical system, demonstrated as the epistemic error dynamics. While we do not explicitly discuss the aleatoric uncertainty due to the stochastic variation related to

intrinsic dynamics, it is implicitly associated with the physical instability of the TGV problem.

The non-linear physical instability can be studied using the developed tools of the disturbance mechanical energy (DME) equation, enstrophy transport equation (ETE), and proper orthogonal decomposition (POD).^{31–33} Here, the DME equation and the disturbance ETE are adopted to numerically study the physical instability of the 2D TGV. Landahl and Mollo-Christensen³⁴ stated that it is possible to study the physical instability from the redistribution of the total mechanical energy. This idea was used to develop a new theory on the growth of DME from the Navier-Stokes equation, without any assumptions, to explain vortex-induced instability.³¹ This DME equation is used here to explain its role for the physical instability in the TGV flow. Doering and Gibbon³⁵ showed that, for 2D periodic flows, the effect of diffusion is strictly dissipative, when viewed globally. However, Sengupta *et al.*³² explained that if diffusion is viewed locally at any instant of time, then it is not strictly dissipative. The authors derived the ETE from the Navier-Stokes equation for inhomogeneous flows and explained the role of diffusion in creating rotationality. The same concept of growth and decay of the disturbance enstrophy has been used in the present study.

This paper is formatted as follows. In the next section, the equilibrium 2D TGV flow is discussed along with the initial condition and the analytical time-dependent solution. The numerical methods used in the present investigation are also defined in this section. In Sec. III, the method of computing the TGV problem is discussed. In Sec. IV, results and discussions are presented, which is followed by Sec. V on the evolution of DME, to follow the deviation of the computed solution from the analytical one. In Sec. VI, the role of the ETE on the evolution of the TGV is discussed. In Sec. VII, the instability via the disturbance ETE is explained for the TGV problem. The paper closes in Sec. VIII, providing the summary and conclusions.

II. THE EQUILIBRIUM 2D TAYLOR-GREEN VORTEX FLOW

The time-dependent 2D incompressible Navier-Stokes equations are solved in the physical-plane using the stream function (ψ) and vorticity (ω) formulation, as given by the stream function equation (SFE) and the vorticity transport equation (VTE),

$$\frac{\partial^2 \psi}{\partial x^2} + \frac{\partial^2 \psi}{\partial y^2} = -\omega, \quad (1)$$

$$\frac{\partial \omega}{\partial t} + u \frac{\partial \omega}{\partial x} + v \frac{\partial \omega}{\partial y} = \frac{1}{Re} \left(\frac{\partial^2 \omega}{\partial x^2} + \frac{\partial^2 \omega}{\partial y^2} \right). \quad (2)$$

The stream function and the velocity are related by $\vec{V} = \nabla \times \vec{\psi}$, with $\vec{\psi} = [0 \ 0 \ \psi]^T$, while the vorticity (ω) is related to the velocity by $\vec{\omega} = \nabla \times \vec{V}$. In the above equations, the components of velocity vector are defined as

$$u = \frac{\partial \psi}{\partial y}, \quad v = -\frac{\partial \psi}{\partial x}. \quad (3)$$

The 2D TGV problem is solved in a periodic domain $0 \leq (x, y) \leq 2\pi$ with the following initial conditions:

$$\psi(x, y, 0) = \sin x \sin y, \quad \omega(x, y, 0) = 2 \sin x \sin y. \quad (4)$$

The computed results are compared with the analytical solution given in terms of the time-dependent ψ and ω , as derived next for the 2D TGV problem. This problem has a solution for ψ and ω given in terms of a time-dependent function, $F(t)$ as

$$\begin{aligned} \psi(x, y, t) &= \sin x \sin y F(t), \\ \omega(x, y, t) &= 2 \sin x \sin y F(t). \end{aligned} \quad (5)$$

Here, $F(t)$ is found out by substituting Eq. (5) in Eq. (2), and upon simplification one gets

$$F(t) = e^{-\frac{2t}{Re}}. \quad (6)$$

This is the analytical time-dependent base flow solution for the 2D TGV problem. It is well known that this equilibrium solution is not stable with respect to omnipresent numerical disturbances, if the Navier-Stokes equation is solved numerically.⁵ The aim of the present study is to see how the numerical solution behaves with respect to the analytical solution and explain such deviations.

The first order spatial derivatives in Eq. (2) (VTE) are discretized using a sixth order, non-uniform compact NUC6-scheme.²⁴ In computing the spatial derivatives by using the compact scheme, periodic boundary conditions have been used in the domain, over the range of 2π in the x - and y -directions of the grid shown in Fig. 1. The second order spatial derivatives in SFE and VTE are obtained by the second order central difference scheme (CD2) for a non-uniform grid.⁴ Additionally, we also report cases, where the second derivatives appearing in the diffusion term of VTE are discretized using the NUC6-scheme applied twice. The four-stage, fourth-order Runge-Kutta method (RK4) is used for the time-integration of VTE. The SFE given by Eq. (1) is solved by the unpreconditioned Bi-CGSTAB³⁶ iterative method, with a tolerance limit of 10^{-7} for convergence.

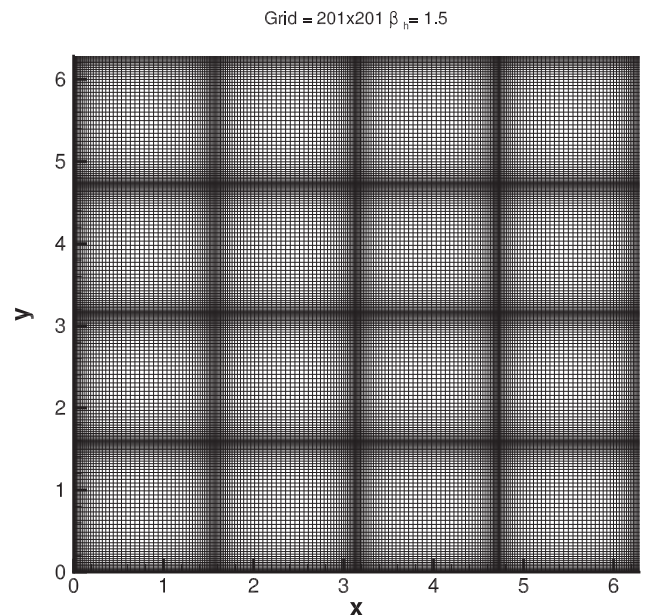


FIG. 1. A sample grid-topology used in the simulations, shown here with 201×201 points and stretching parameter $\beta_n = 1.5$.

III. COMPUTATION OF THE 2D TAYLOR-GREEN VORTEX

The simulations presented here are as listed in Table I. A square domain of length 2π has been chosen, constituting a basic unit of four TGV cells, with a full-saddle point³⁷ at the center of the domain. This arrangement shows a breakdown of symmetry due to the growth of disturbances. Due to the combined actions of vorticity gradient terms and the growth of disturbance quantities, the disturbance vorticity grows with time. The grid is defined with a tangent-hyperbolic double-sided distribution⁴ in the x - and the y -directions. Given a uniform distribution of points between 0 and $l = \pi/2$ by η_i in the transformed plane, with $i = 1$ to $i = N/4$, and β_h as the stretching parameter, the nodes x_i in the physical plane are given by

$$x_i = \frac{l}{2} \left[1 - \frac{\tanh \beta_h (1 - 2\eta_i)}{\tanh \beta_h} \right]. \quad (7)$$

This same grid spacing is used as a mirror image in the adjacent segment, i.e., from $i = N/4 + 1$ to $i = N/2$, and so on, up to $i = N$, so that the grid has finer spacing, where the solution gradients involved in Eqs. (1) and (2) are high, namely, near the boundary of the domain, at the core of the vortices and at the saddle point. An identical grid distribution is used in the y -direction. A typical topology of the grid with (201×201) points, and $\beta_h = 1.5$ is shown in Fig. 1.

A time step (Δt) of 10^{-4} is chosen such that, for all the cases in Table I, the maximum and minimum

TABLE I. Numerical parameters of the test cases reported are shown here.

Case	Grid	h_{max}	h_{min}	N_{cmin}	N_{cmax}	Pe_{min}	Pe_{max}	Re
1	401×401	0.026	0.0048	0.0038	0.0206	0.00029	0.00868	500
2	401×401	0.026	0.0048	0.0038	0.0206	0.00007	0.00213	2000
3	401×401	0.026	0.0048	0.0038	0.0206	0.00001	0.00043	10^4

Courant-Friedrichs-Lewy (CFL) numbers (N_{cmin} , N_{cmax}) and Peclet numbers (Pe_{min} , Pe_{max}) lie within the region where the non-dimensional numerical amplification factor ($|G_{num}|/|G_{phys}|$) is very close to unity for the NUC6-scheme.²⁴ Here, G_{phys} is the physical amplification factor and G_{num} is the numerical amplification factor for the model 1D convection-diffusion equation, as analyzed in the work of Suman *et al.*³⁸ Here, $N_{cmin} = \frac{\Delta t}{h_{max}}$, $N_{cmax} = \frac{\Delta t}{h_{min}}$, $Pe_{min} = \frac{1}{Re} \frac{\Delta t}{h_{max}^2}$, and $Pe_{max} = \frac{1}{Re} \frac{\Delta t}{h_{min}^2}$, where h_{max} is the coarsest grid spacing and h_{min} is the finest grid spacing in the entire domain. The stretching parameter, $\beta_h = 1.5$, is used for all the computations reported here.

IV. RESULTS AND DISCUSSION

Figure 2 compares the numerical solution (solid lines) with the analytical solution (dashed lines) for non-dimensional times of $t = 50$ and 150 , for case-1 listed in Table I. The numerical solution matches with the exact solution at these times. Also, the root mean square (RMS) error for ψ and ω is shown

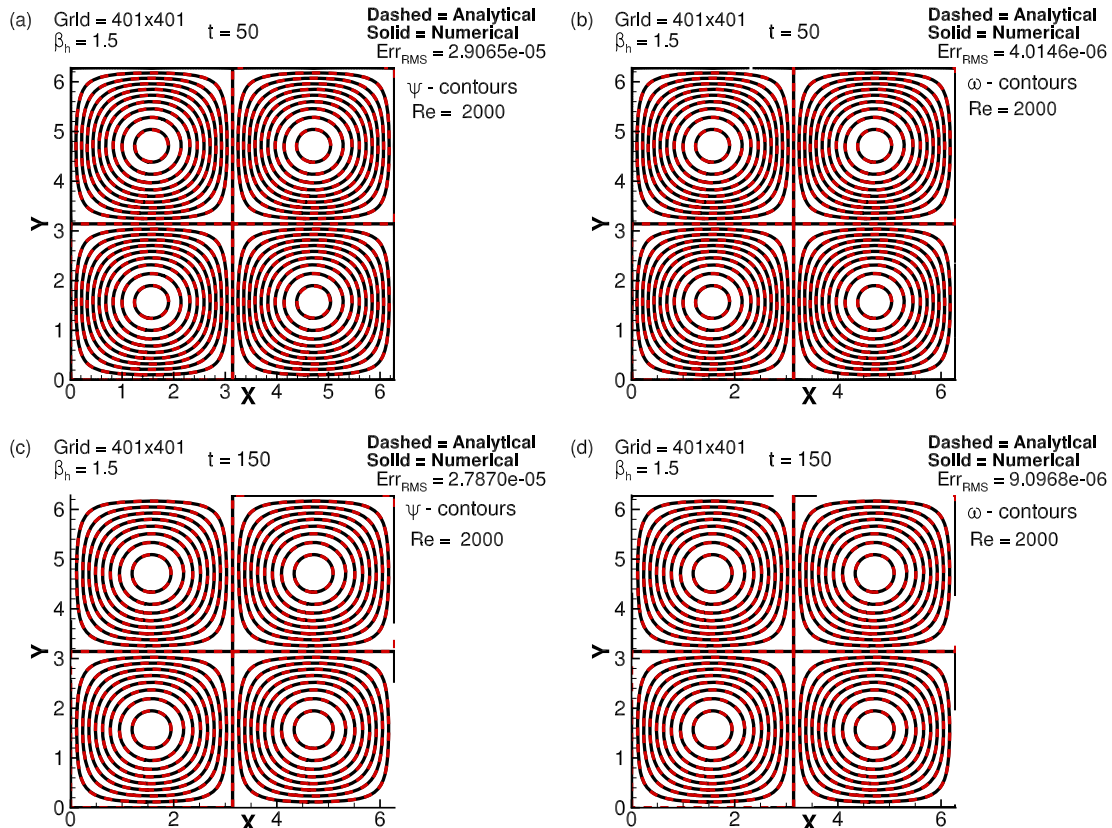


FIG. 2. Comparison of the numerical results (solid line) with the analytical solution (dashed line) shown at $t = 50$ in frames (a) and (b) and at $t = 150$ in frames (c) and (d). Contours of ψ are shown in frames (a) and (c), and ω -contours are in frames (b) and (d) for $Re = 2000$ (case-1 of Table I).

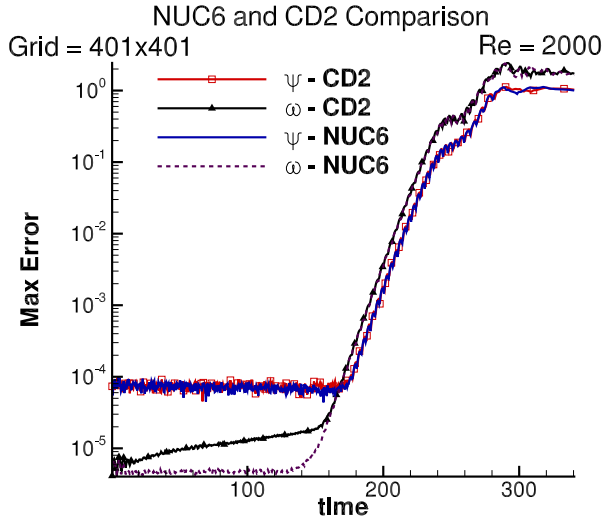


FIG. 3. Comparison of the maximum error in ψ and ω obtained using the CD2 scheme in the non-uniform grid and NUC6-scheme applied twice for the diffusion terms in Eq. (2) for case-1.

in the figure. The expressions for these RMS quantities are given below for the stream function, with ψ_A and ψ_N representing analytical and numerical values, respectively, and N is the number of grid points in the x - and the y -directions,

$$Err_{RMS} = \sqrt{\frac{\sum_{j=1}^N \sum_{i=1}^N (\psi_N(i,j) - \psi_A(i,j))^2}{N * N}}. \quad (8)$$

The RMS errors are of the order 10^{-5} for ψ and 10^{-6} for ω , as indicated in Fig. 2. It is noted that the solution loses symmetry above $t \cong 160$.

Figure 3 shows the maximum error in ψ and ω , when the diffusion terms in Eq. (2) are computed using the CD2 scheme in the non-uniform grid,⁴ and using the NUC6-scheme²⁴ applied twice. The difference in the maximum error for these two schemes for discretizing the diffusion term is very small. Therefore, we conclude that there is a very weak dependence of the results on the methods used for discretizing the highest order derivatives, i.e., the diffusion terms.

At around $t = 220$, the four vortices start convecting while losing coherence, as shown in Fig. 4. These vortices eventually fragment into small structures at later times.

The magnitude of the maximum error for ω , denoted as $(\omega_d)_{max} = \text{maximum}(|\omega_A - \omega_N|)$, is plotted in a log scale as a function of time for $Re = 500$ (case-2), 2000 (case-1), and 10 000 (case-3) in Fig. 5. The maximum amplitude of the error remains nearly constant up to $t = 160$ for higher Re cases, whereas for $Re = 500$ it remains nearly constant up to $t = 310$, after which the error increases. For lower Re cases, the flow is dominated by diffusion over convection, where stronger diffusion suppresses disturbances. Thus, the flow remains stable for a longer time for lower Re cases. The error during initial transient stages is higher for $Re = 500$ because the operational Pe -range is highest for the lowest Re . From the results in Fig. 5, it is observed that for all the cases, the numerical solution remains stable up to $t = 160$, and following which, the solution becomes destabilized, evident from the breakdown of symmetry of the original (2×2) cells of vortices. The trajectory of $\frac{d\omega}{dt}$ with respect to ω in phase space for the full saddle point is plotted in Fig. 6. Different marked points in the figure indicate the various stages of instability, as shown by the vorticity at the full saddle point; break down of original symmetry of the TGV and nonlinear saturation of the

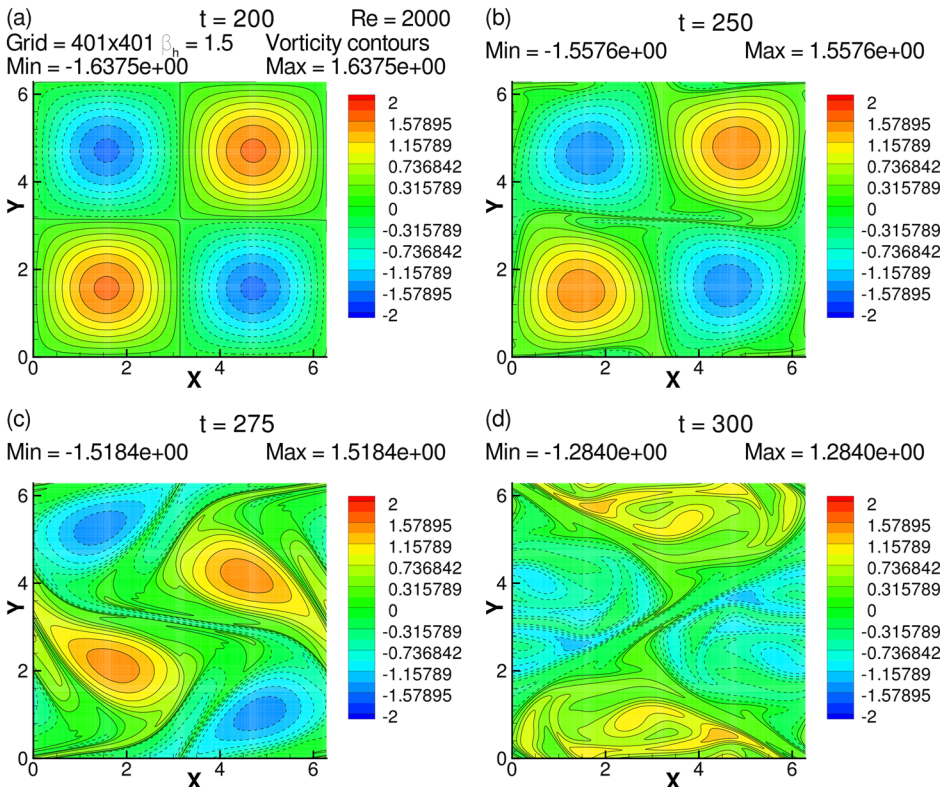


FIG. 4. Vorticity (ω) contours at indicated non-dimensional times for case-1.

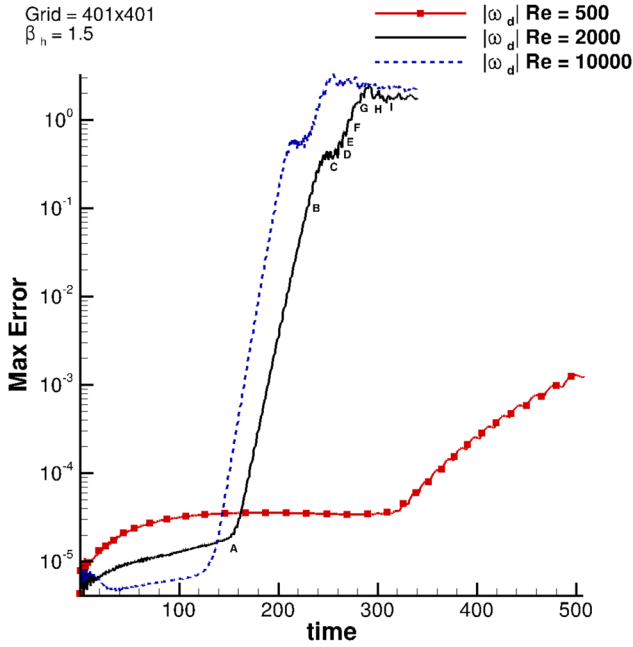


FIG. 5. Amplitude of $(\omega_d)_{max}$ plotted in a log scale as a function of time for the cases in Table I, for $Re = 500, 2000,$ and $10\,000$.

disturbance vorticity at the saddle point with the corresponding points are shown in Fig. 5. Point A indicates the onset of instability with $\frac{d\omega}{dt}$ of the order of 10^{-5} , after which the magnitude of $\frac{d\omega}{dt}$ rapidly starts increasing. In Fig. 5 at around $t = 252.60$, we have already noted that the point C shows a small dip in the temporal growth rate. After which the magnitude again increases, with fluctuations at points D–H. The point I marks the nonlinear saturation of growth, after which the magnitude of $\frac{d\omega}{dt}$ remains constant. It is noted that, though the instabilities arise physically here, these are triggered by numerical errors. The reasons behind the appearance of instabilities and the breakdown of vortices are explained by the DME and the disturbance ETE, in the following sections.

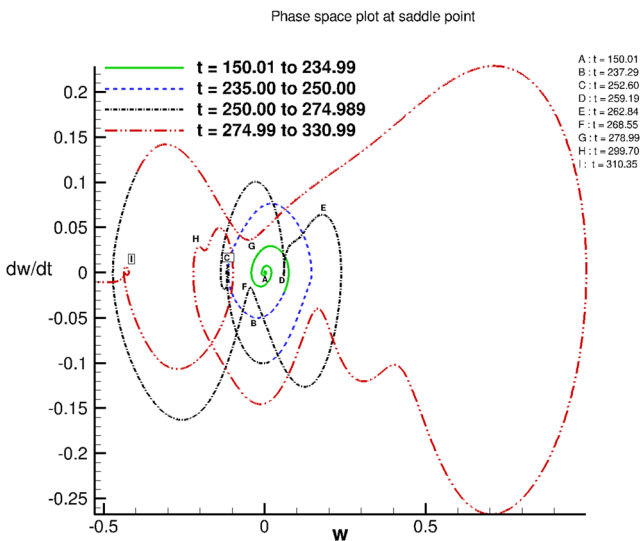


FIG. 6. Phase space trajectory of $\frac{d\omega}{dt}$ vs ω at the saddle point for case 2 ($Re = 2000$) of Table I.

V. EVOLUTION OF DME AND LOSS OF COHERENCE OF THE TAYLOR-GREEN VORTICES

It is essential to study the roles of various parameters responsible for the onset of asymmetry (by which we mean the loss of coherence of the TGV) from the perfectly symmetric initial state. As emphasized by Landahl and Mollo-Christensen,³⁴ the total mechanical energy is a parameter which can provide a clue to the onset of instability. The use of the total mechanical energy to study nonlinear disturbance growth in flows has been explained by Sengupta *et al.*³¹ Here, we analyze the loss of symmetry, by computing the DME equation,³¹ as described next. The equation for the total mechanical energy $E = \frac{p}{\rho} + \frac{\vec{V} \cdot \vec{V}}{2}$ is obtained by taking divergence of the rotational form of the Navier-Stokes equation and is given as follows:

$$\nabla^2 E = \vec{\omega} \cdot \vec{\omega} - \vec{V} \cdot (\nabla \times \vec{\omega}). \quad (9)$$

The right-hand side of Eq. (9) shows how the vorticity ($\vec{\omega}$) and the velocity (\vec{V}) vectors interact to create mechanical energy. We split the instantaneous variables in Eq. (9) into the equilibrium and the perturbation quantities as³¹ $E = E_m + \epsilon E_d$; $\vec{V} = \vec{V}_m + \epsilon \vec{V}_d$; $\vec{\omega} = \vec{\omega}_m + \epsilon \vec{\omega}_d$, where subscripts m and d represent the time-dependent base flow and disturbance components of the flow, respectively. We get the equilibrium mechanical energy from

$$\nabla^2 E_m = \vec{\omega}_m \cdot \vec{\omega}_m - \vec{V}_m \cdot (\nabla \times \vec{\omega}_m). \quad (10)$$

Substituting the above expressions in Eq. (9), one gets

$$\begin{aligned} \nabla^2 E_d = & 2\vec{\omega}_m \cdot \vec{\omega}_d + \epsilon \vec{\omega}_d \cdot \vec{\omega}_d - \vec{V}_m \cdot (\nabla \times \vec{\omega}_d) \\ & - \vec{V}_d \cdot (\nabla \times \vec{\omega}_m) - \epsilon \vec{V}_d \cdot (\nabla \times \vec{\omega}_d). \end{aligned} \quad (11)$$

Here, the analytical solution is used as the time-dependent base flow, and the numerical solution is the instantaneous quantity. Therefore,

$$\begin{aligned} \vec{\omega}_m &= \omega_A \hat{k}, & \vec{\omega}_d &= (\omega_N \hat{k} - \omega_A \hat{k}), \\ \vec{V}_m &= u_A \hat{i} + v_A \hat{j}, & \vec{V}_d &= (u_N - u_A) \hat{i} + (v_N - v_A) \hat{j}, \end{aligned}$$

where subscript A corresponds to the analytical solution and subscript N represents the numerical solution. Equation (11) is a Poisson equation with non-zero right-hand side (RHS) representing either a source or a sink of disturbance energy in the domain. A positive RHS acts as a sink and a negative RHS acts as a source of disturbance energy.^{31,39} The RHS of the DME equation in Eq. (11) consists of the following five terms:

$$\begin{aligned} T_1 &= 2\vec{\omega}_m \cdot \vec{\omega}_d, & T_2 &= \vec{\omega}_d \cdot \vec{\omega}_d, \\ T_3 &= -\vec{V}_m \cdot (\nabla \times \vec{\omega}_d), & T_4 &= -\vec{V}_d \cdot (\nabla \times \vec{\omega}_m), \end{aligned}$$

and

$$T_5 = -\vec{V}_d \cdot (\nabla \times \vec{\omega}_d).$$

Terms (T_1) and (T_2) on the RHS of the DME equation are due to interactions of the equilibrium and disturbance vorticity fields ($\vec{\omega}_m \cdot \vec{\omega}_d$) and the self-interacting non-linear term ($\vec{\omega}_d \cdot \vec{\omega}_d$). Other terms (T_3 , T_4 , and T_5) are due to interactions of the velocity and vorticity dependent terms.

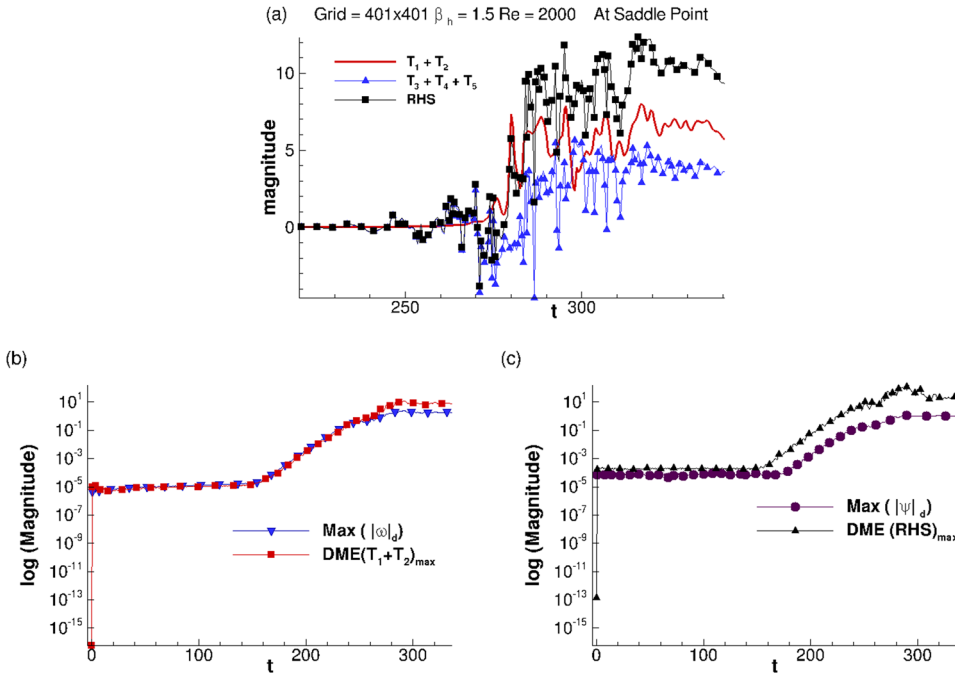


FIG. 7. (a) Variation of terms $(T_1 + T_2)$, $(T_3 + T_4 + T_5)$ and the total RHS of DME equation at the full saddle point, plotted with respect to time. (b) Comparison of the maximum amplitude of error in ω (nabla symbol) with $(T_1 + T_2)$ on the RHS of the DME equation (square); (c) comparison of the maximum error amplitude of ψ (circle) and the RHS of the DME equation (delta), plotted vs. time for $Re = 2000$ using $\Delta t = 10^{-4}$ (case-1).

In Fig. 7, the variation of various terms $(T_1 + T_2)$, $(T_3 + T_4 + T_5)$ in the RHS of DME and the total RHS of DME Eq. (11), with respect to time is shown in frame (a). It is observed that the contributions from terms T_3 , T_4 , and T_5 are small, as compared to that coming from T_1 and T_2 . The terms T_3 , T_4 , and T_5 represent interactions between velocity and palinstrophy $(\nabla \times \vec{\omega})$ dependent terms, whereas terms T_1 and T_2 represent the interactions of the equilibrium and disturbance vorticity fields or the disturbance enstrophy. The maximum positive value of $(T_1 + T_2)$ and the amplitude of maximum disturbance vorticity $|\omega_d|$ are plotted in frame (b). The evolution of the maximum value of the RHS of the DME equation and the amplitude of the maximum disturbance stream function $|\psi_d|$ is shown in frame (c) for case-1. The stream function represents the global integrated flow field, and it follows the $(RHS)_{\text{max}}$ of the DME equation. The value of $(T_1 + T_2)$ matches well with the maximum- $|\omega_d|$ plot. We can see from the figure that $(T_1 + T_2)$ and the RHS of the DME equation remain nearly constant up to $t = 160$. After this, the vortices convect, break down, and lose complete coherence, resulting in an increase of the maximum value of $(T_1 + T_2)$ and the RHS.

VI. ROLE OF THE ETE ON THE EVOLUTION OF THE TAYLOR-GREEN VORTICES

The ETE is obtained by taking the inner product of the VTE with $\vec{\omega}$ and is given for 3D flows as³²

$$\frac{\partial \Omega_1}{\partial t} + u_j \frac{\partial \Omega_1}{\partial x_j} - 2\omega_i \omega_j \frac{\partial u_i}{\partial x_j} = \frac{1}{Re} \frac{\partial^2 \Omega_1}{\partial x_j \partial x_j} - \frac{2}{Re} \left(\frac{\partial \omega_i}{\partial x_j} \right) \left(\frac{\partial \omega_i}{\partial x_j} \right). \quad (12)$$

The ETE gives an estimate of the growth or decay of the enstrophy (Ω_1) with time for any arbitrary inhomogeneous flow. The distinction between the diffusion and dissipation for inhomogeneous flows was clarified with the help of the

ETE,³² where it was demonstrated that for inhomogeneous flows, the diffusion term can be simplified into two sets of terms. The second set of terms on the RHS of Eq. (12) is strictly negative, and hence, it is dissipative in nature. The first term in the RHS of the ETE can either be positive or negative. The sign of the RHS of the ETE given by Eq. (12) depends upon the diffusion terms $(\frac{\partial^2 \Omega_1}{\partial x_j \partial x_j})$ and thus plays an important role in creating or destroying rotationality.

As the vortex stretching term is completely absent for 2D flows, the third term on the left-hand side of Eq. (12) disappears and one gets

$$\frac{\partial \Omega_1}{\partial t} + u_j \frac{\partial \Omega_1}{\partial x_j} = \frac{1}{Re} \frac{\partial^2 \Omega_1}{\partial x_j \partial x_j} - \frac{2}{Re} \left(\frac{\partial \omega}{\partial x_j} \right) \left(\frac{\partial \omega}{\partial x_j} \right).$$

The simplified equation for 2D flows in the Cartesian frame is given as

$$\frac{D\Omega_1}{Dt} = \frac{1}{Re} \left[\frac{\partial^2 \Omega_1}{\partial x^2} + \frac{\partial^2 \Omega_1}{\partial y^2} \right] - \frac{2}{Re} \left[\left(\frac{\partial \omega}{\partial x} \right)^2 + \left(\frac{\partial \omega}{\partial y} \right)^2 \right]. \quad (13)$$

In Eq. (13), Ω_1 is a strictly positive term and a positive RHS implies that diffusion causes numerical growth, whereas a negative RHS would mean decay of Ω_1 . In Fig. 8, we show the RHS of Eq. (13) for the ETE evaluated at $t = 160$ for $Re = 2000$. According to Fig. 5, this is the time at which the error increases exponentially. It has been stated in the work of Doering and Gibbon³⁵ that for the 2D periodic flow, the enstrophy decreases monotonically in the whole domain. However, in their analysis,³⁵ the instability of the enstrophy has not been considered. In Fig. 8(a), the analytically obtained RHS of the ETE [Eq. (13)] is observed to be negative everywhere in the domain, which is expected for the global integrated property without any instability.³⁵ However, the numerical solution shows the growth of disturbances, which is estimated from the RHS of Eq. (13) and shown in Fig. 8(b).

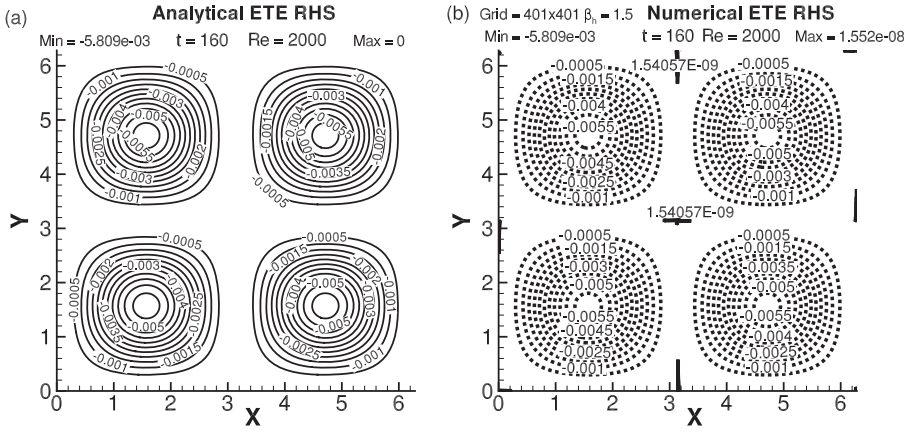


FIG. 8. Contours of the RHS of the ETE for (a) the analytical solution and (b) the computed solution at $t = 160$, for a grid with $\beta_h = 1.5$ and $Re = 2000$. Positive value of the RHS of the ETE is shown by the continuous lines, as shown in frame (b).

The numerical RHS shows regions of growth of the enstrophy, as marked by continuous lines in the figure. Hence, despite the equilibrium flow being 2D and periodic, the flow experiences a loss of symmetry due to the growth of rotationality at different scales in the domain. The present simulations show the creation of small-scale eddies associated with the loss of symmetry due to the physical instability. These small-scale eddies are inhomogeneous and are formed in regions where strain dominates vorticity.⁴⁰ Figure 9 shows the evolution of the maximum values of the RHS of the ETE; $E_1 = \frac{1}{Re} \left[\frac{\partial^2 \Omega_1}{\partial x^2} + \frac{\partial^2 \Omega_1}{\partial y^2} \right]$ and $E_2 = \frac{2}{Re} \left[\left(\frac{\partial \omega}{\partial x} \right)^2 + \left(\frac{\partial \omega}{\partial y} \right)^2 \right]$, for case-1. It is observed from the figure that $\max(\text{RHS})$ of the ETE is positive and increases with time due to a non-linear instability. The maximum value of RHS of the ETE is of $O(10^{-17})$ for $t < 100$, which is below the machine-zero and not shown by the post-processor.

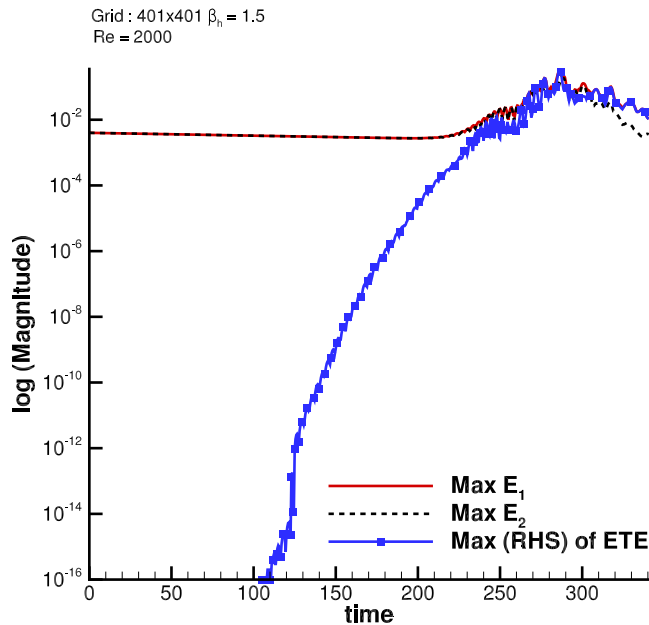


FIG. 9. Time evolution of the maximum value of the RHS of the ETE, maximum of terms $E_1 = \frac{1}{Re} \left[\frac{\partial^2 \Omega_1}{\partial x^2} + \frac{\partial^2 \Omega_1}{\partial y^2} \right]$ and $E_2 = \frac{2}{Re} \left[\left(\frac{\partial \omega}{\partial x} \right)^2 + \left(\frac{\partial \omega}{\partial y} \right)^2 \right]$ plotted in a log scale for $Re = 2000$. Below $t = 100$, the maximum value of the RHS is of the order of 10^{-17} .

VII. INSTABILITY OF THE ENSTROPY TRANSPORT EQUATION

Doering and Gibbon³⁵ have shown that for 2D periodic flows the enstrophy integrated over the full domain decreases monotonically, but the instability of the enstrophy was not considered. Here, an instability analysis of the enstrophy is presented, showing the linear and non-linear growth rates.⁴¹ As mentioned earlier, the analytical solution is considered as the time-dependent base flow and numerical solution as the instantaneous solution. Therefore, we split the instantaneous variables in Eq. (13), into an equilibrium and a perturbation quantity as $\Omega_1 = \Omega_m + \epsilon_1 \Omega_d$; $u = u_m + \epsilon_2 u_d$; $v = v_m + \epsilon_2 v_d$; $\omega = \omega_m + \epsilon_2 \omega_d$, where subscripts m and d represent the time-dependent base flow and disturbance components, respectively. The relation between ϵ_1 and ϵ_2 is given by $\epsilon_1 = 2 * \epsilon_2$. Substituting the above in Eq. (13) and collecting $O(\epsilon_1)$ terms, one gets

$$\frac{D\Omega_d}{Dt} = \frac{1}{Re} \left[\frac{\partial^2 \Omega_d}{\partial x^2} + \frac{\partial^2 \Omega_d}{\partial y^2} \right] - \frac{2}{Re} \left[\left(\frac{\partial \omega_m}{\partial x} \right) \left(\frac{\partial \omega_d}{\partial x} \right) + \left(\frac{\partial \omega_m}{\partial y} \right) \left(\frac{\partial \omega_d}{\partial y} \right) \right]. \quad (14)$$

The above equation gives the linearized growth of the disturbance enstrophy. Here, the contribution of the last term on the RHS of the above equation can cause decay or growth of Ω_d , unlike what is observed for the total enstrophy. The total enstrophy Ω_1 is positive definite, whereas Ω_d is given as $\Omega_d = \vec{\omega}_d \cdot \vec{\omega}_m$, i.e., it is due to the interaction between the equilibrium and the disturbance vorticity fields, and hence it can be either positive or negative. Figure 10 shows the time evolution of the disturbance enstrophy Ω_d and the mean enstrophy Ω_m , summed over the full domain, using $\Delta t = 10^{-4}$ for $Re = 2000$, in frames (a) and (b), respectively. Frame (b) shows that the integrated mean enstrophy decays with time, which is consistent with the property of the equilibrium flow.³⁵ Whereas the variation of the integrated disturbance enstrophy with time in frame (a) shows that initially the integrated Ω_d remains close to zero, and at $t = 210$ when vortices start breaking down, its amplitude increases sharply and thereafter fluctuates about a constant value.

The points in the domain where $\Omega_d > 0$ and $D\Omega_d/Dt > 0$ are the locations for growth of disturbances. Similarly, if at

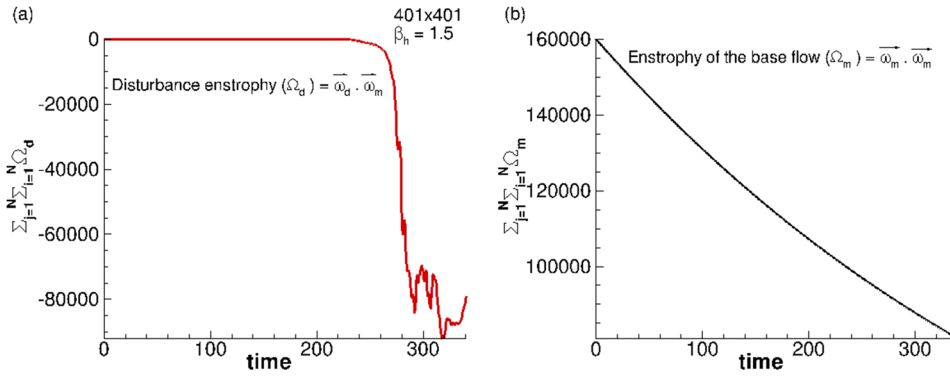


FIG. 10. Comparison of the evolution of (a) the disturbance enstrophy Ω_d and (b) enstrophy of the base flow, Ω_m , summed over the whole domain, as shown for $\Delta t = 10^{-4}$ and $Re = 2000$.

a place where $\Omega_d < 0$, if $D\Omega_d/Dt$ is negative, then we have instability locally, as the amplitude of Ω_d increases with time for both the cases. Therefore, the instability is indicated by the

signs of Ω_d and the substantive derivative, $D\Omega_d/Dt$. The non-linear growth of the disturbance enstrophy can be obtained by subtracting the ETE for the equilibrium flow from the

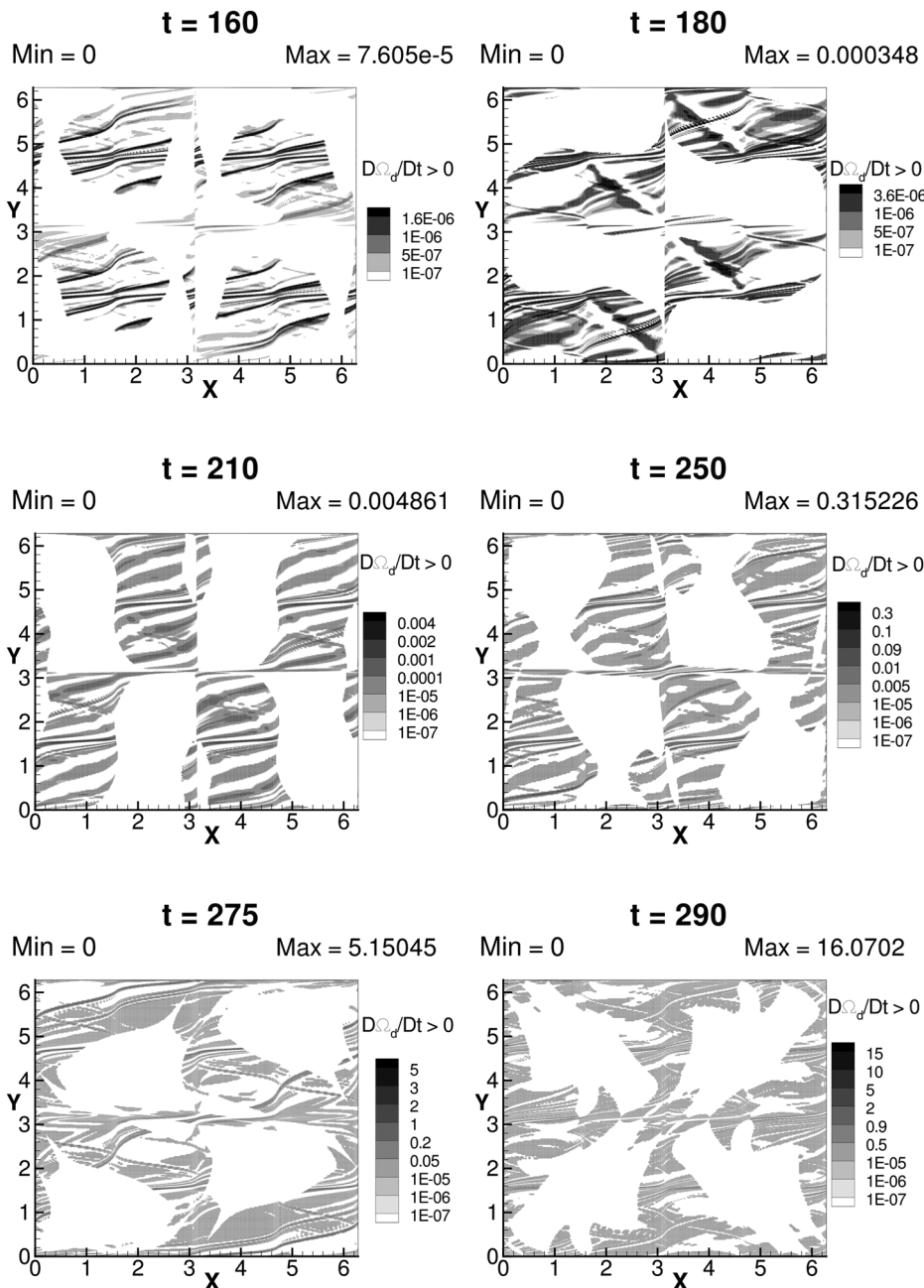


FIG. 11. Contours of the RHS of the disturbance enstrophy transport equation, Eq. (14), ($\frac{D\Omega_d}{Dt} > 0$) and ($\Omega_d > 0$) for the linearized growth rate, shown at the indicated times, for $\Delta t = 10^{-4}$ and $Re = 2000$.

instantaneous ETE. Writing the instantaneous ETE as

$$\frac{D\Omega_1}{Dt} = \frac{1}{Re} \left[\frac{\partial^2 \Omega_1}{\partial x^2} + \frac{\partial^2 \Omega_1}{\partial y^2} \right] - \frac{2}{Re} \left[\left(\frac{\partial \omega}{\partial x} \right)^2 + \left(\frac{\partial \omega}{\partial y} \right)^2 \right]. \quad (15)$$

The ETE for the equilibrium flow is

$$\frac{D\Omega_m}{Dt} = \frac{1}{Re} \left[\frac{\partial^2 \Omega_m}{\partial x^2} + \frac{\partial^2 \Omega_m}{\partial y^2} \right] - \frac{2}{Re} \left[\left(\frac{\partial \omega_m}{\partial x} \right)^2 + \left(\frac{\partial \omega_m}{\partial y} \right)^2 \right]. \quad (16)$$

Subtracting Eq. (16) from Eq. (15), one gets the nonlinear growth rate for Ω_d as

$$\frac{D\Omega_d}{Dt} = R_1 - R_m, \quad (17)$$

where R_1 and R_m represent the RHS of Eqs. (15) and (16), respectively.

In Figs. 11 and 12, the linear growth rate contours of the disturbance enstrophy given by Eq. (14) are shown at the indicated times of $t = 160, 180, 210, 250, 275,$ and 290 . Figure 11 shows the region where Ω_d along with its time rate are positive. Similarly, Fig. 12 shows the region where Ω_d along with its time rate are negative. Both these conditions are indicative of instability for the disturbance enstrophy, i.e., the positive value increases, while the negative value becomes more and more negative. The start-up time in these figures is understood, by looking at Fig. 5, which shows that up to $t = 160$, the disturbance quantity virtually remains zero, as it is also seen in Fig. 10 for Ω_d , for even a longer duration.

It is observed that at the onset of growth ($t = 160$ and 180), the RHS of Eq. (14) indicating the growth rate has a global maximum at the core of the vortices, at the full saddle point, and along the dividing lines of the vortical cells. The growth rate of Ω_d grows by orders of magnitude in the frame at $t = 210$,

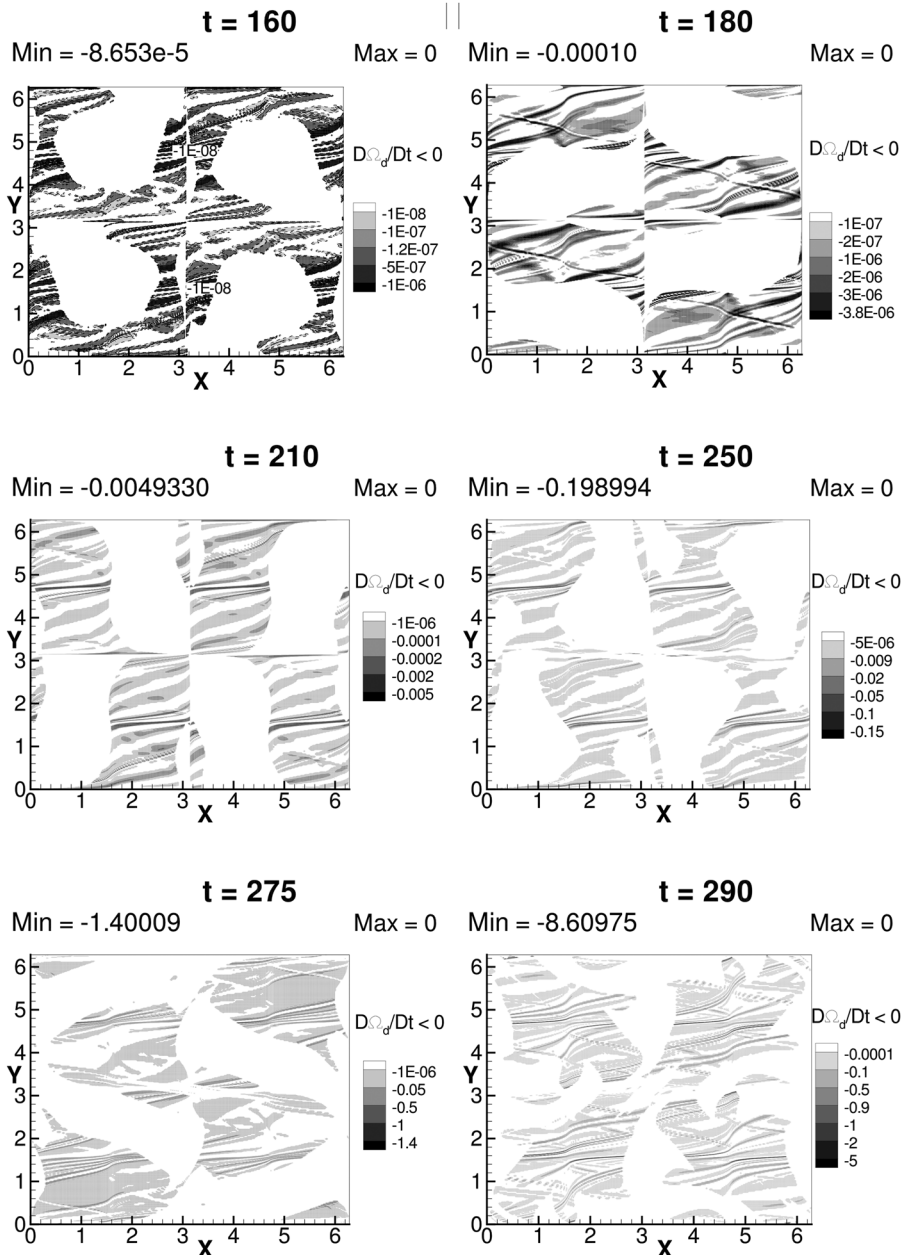


FIG. 12. Contours of the RHS of the disturbance enstrophy transport equation, Eq. (14), ($\frac{D\Omega_d}{Dt} < 0$) and ($\Omega_d < 0$) for the linearized growth rate, shown at the indicated times, for $\Delta t = 10^{-4}$ and $Re = 2000$.

as compared to the frames at $t = 160$ and 180 in Figs. 11 and 12, and which again increases by another order of magnitude by $t = 250$. During these times, the maximum growth rate for positive Ω_d is along the horizontal streaks from the cores to the edge of the cells (toward the right in the top cells and toward the left for the bottom cells). For negative Ω_d , these streaks of maximum growth rate are in complimentary directions, i.e., on the top cells the streaks are from the core to the left and from the core to the right for the bottom cells. Subsequent frames at later times also show continuing growth, with the maximum growth rates noted near the cell boundaries, and not near the core for $\Omega_d > 0$. For negative Ω_d , the maximum growth rates at later time frames are along the horizontal streaks passing through the vortex core for the linearized growth rates.

The corresponding non-linear growth of Ω_d is shown in Figs. 13 and 14, at the indicated times of $t = 160, 180, 210, 250, 275,$ and 290 . As in Figs. 11 and 12 for the linearized growth rate, here also we have two possibilities, depending upon the sign of Ω_d . The $(D\Omega_d/Dt > 0)$ -contours plotted in

Fig. 13 show regions of instability, for the case of $\Omega_d > 0$. Similarly, the instability of $\Omega_d < 0$ is shown in Fig. 14. For the positive Ω_d , the onset is noted at the cores (seen for $t = 160$ and 180), which at $t = 210$ shows the site of maximum growth to be near the dividing lines of the vortical cells. From the bottom two frames (at $t = 275$ and 290), one notices periodic symmetry in alternate cells in both the horizontal and vertical directions, about the full saddle point. It is also remarkable to note that the non-linear growth rates are orders of magnitude lower at later times, as compared to the linear growth rates shown in Fig. 11. For the negative Ω_d case also, the nonlinear growth rates are significantly lower by orders of magnitude at later times, as compared to the linear growth rate shown in Fig. 12.

From Figs. 10–14, it is apparent that the error evolution studied here is due to cumulative background disturbances, which is not due to any imposed excitations. From Fig. 10, it is evidently clear that the disturbance enstrophy remains at machine zero up to $t \approx 210$, which thereafter grows rapidly,

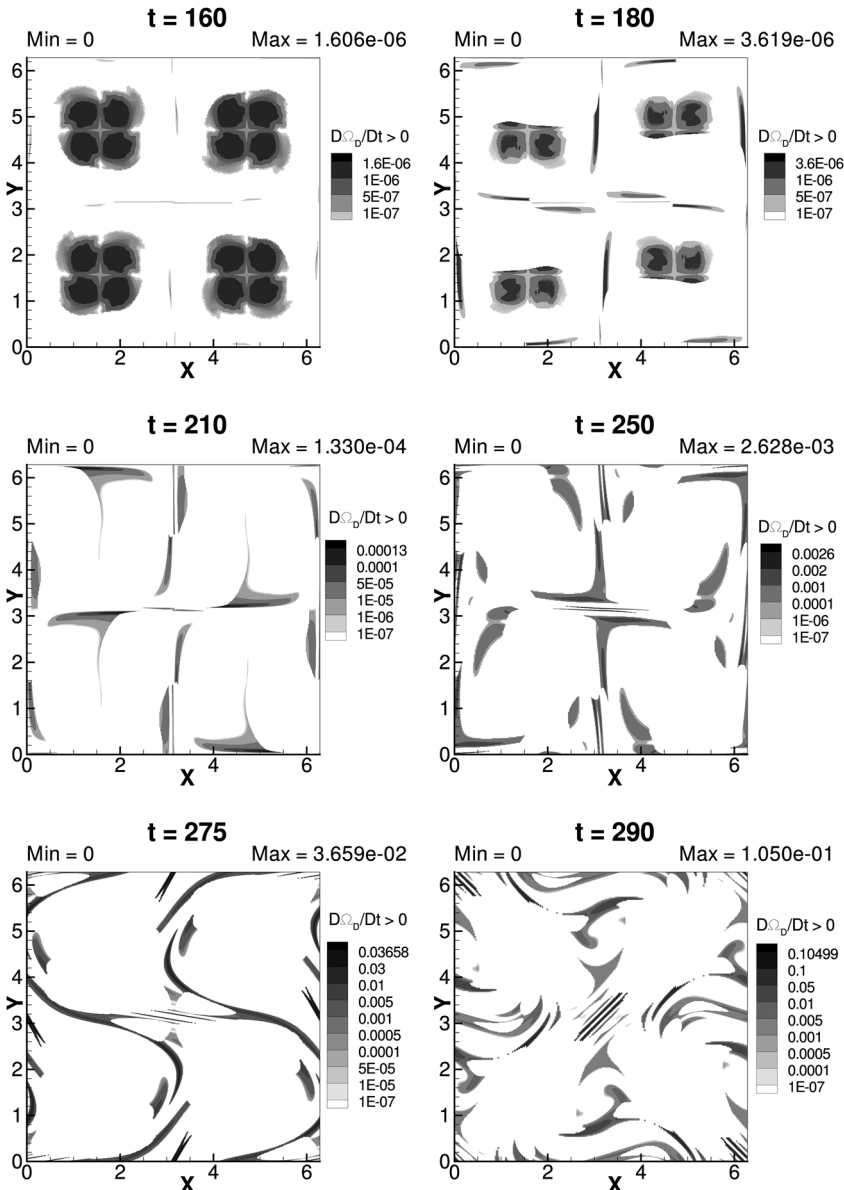


FIG. 13. Contours of the RHS of the non-linear growth rate of the disturbance enstrophy transport equation, Eq. (17), $(\frac{D\Omega_d}{Dt} > 0)$ and $(\Omega_d > 0)$, shown at the indicated times, for $\Delta t = 10^{-4}$ and $Re = 2000$.

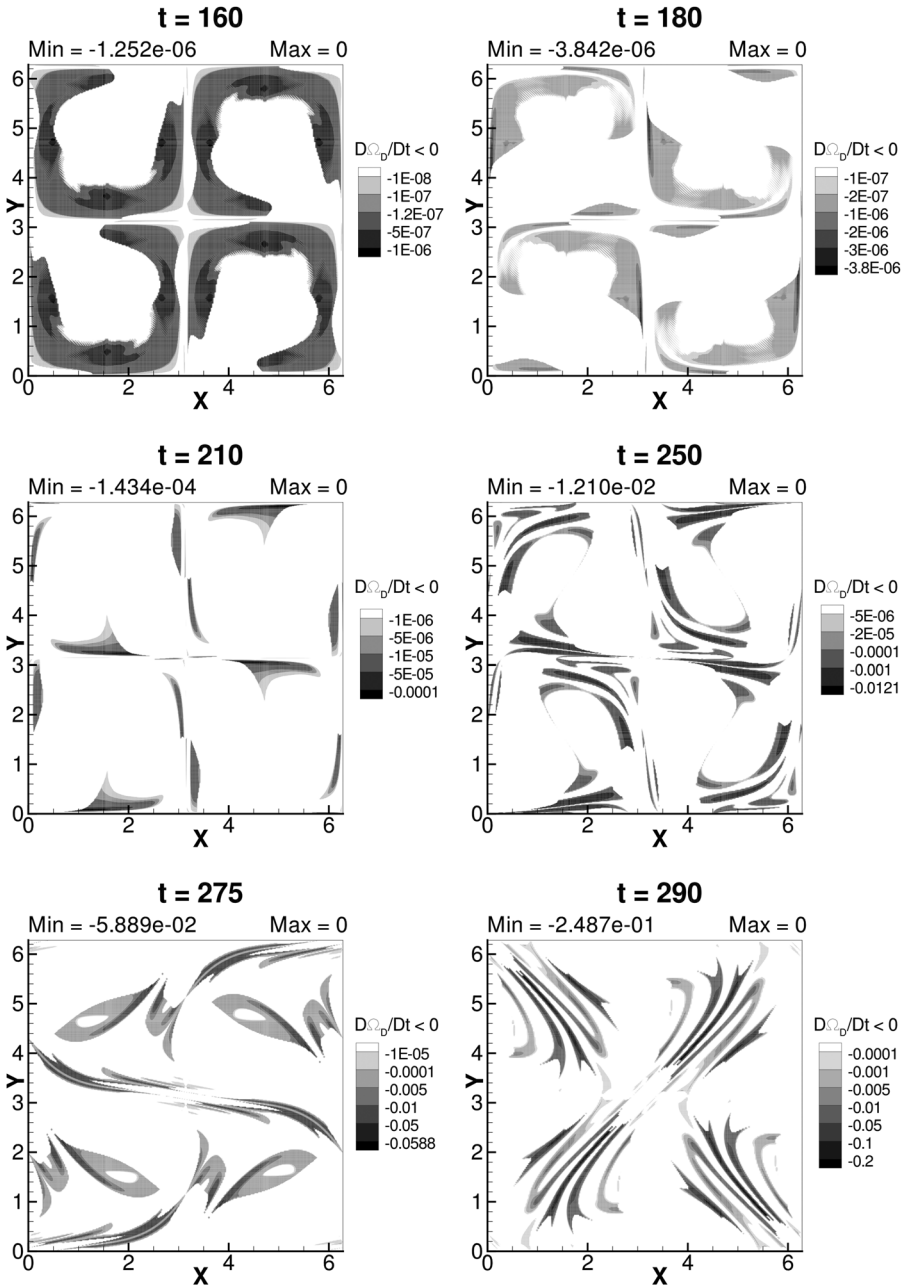


FIG. 14. Contours of the RHS of the non-linear growth rate of the disturbance enstrophy transport equation, Eq. (17), ($\frac{D\Omega_d}{Dt} < 0$) and ($\Omega_d < 0$), shown at the indicated times, for $\Delta t = 10^{-4}$ and $Re = 2000$.

and that can be traced by the present linear/non-linear theory based on DNS results. Thus, the instabilities are triggered by numerical noises and not by any deterministic excitation. In existing linear theory,³ the TGV problem itself is changed, where the circular vortices have been made to elliptic vortices so that the developed theory of elliptic instability can be used. Second, the boundary conditions employed in this linear theory impose conditions on the edge of the vortical cells, to study the so-called symmetry of disturbances, while not employing the periodic boundary conditions. Thus, in a true sense, there is no linear theory to study the TGV problem.

VIII. SUMMARY AND CONCLUSION

In the present research, we have analyzed the instability of the 2D TGV flow by performing DNS of the Navier-Stokes

equation, using (ψ, ω) -formulation, with a non-uniform grid, for three different Reynolds numbers. The 2D TGV double-periodic problem has an analytical solution, which can be treated as the time-dependent base flow solution. However, the numerical solution of the Navier-Stokes equation with the periodic initial condition is noted to suffer deviations from this analytical solution after a moderate span of time, and this has remained unexplained so far. For this time-dependent base flow solution, these deviations are explained via the study of the instability using the tools of the total mechanical energy and the enstrophy transport equation.^{31,32} Both these tools have been developed from the Navier-Stokes equation without any assumption and are thus capable of explaining such deviations for an inhomogeneous, incompressible flow. This analysis should also be valid for general incompressible flows.

One of the events noted here in a domain consisting of four TGVs is, when the four initial vortices start moving and fragmenting, breaking down the symmetry, as shown in frames (c) and (d) of Fig. 4. In Sec. V, the nonlinear evolution of disturbances is explained in terms of the DME equation given by Eq. (11), by identifying regions, classified as sources and sinks of the DME.³¹ The other identification tool for tracking the evolution of disturbances is through the ETE, as given in Eq. (12), which is derived to explain the creation of rotationality in 2D and 3D inhomogeneous flows following the efforts of Sengupta *et al.*³²

In the absence of stretching, the time derivative of the total enstrophy for 2D flow is determined by the sign of the RHS of Eq. (13). A positive RHS corresponds to the creation of rotationality, while negative RHS is related to the decay of enstrophy in time. In general for 2D periodic flows, the total enstrophy in the domain should be a decaying function of time,³⁵ only in the absence of physical instabilities. However, the numerical error in the present work drives the time-dependent base flow in isolated regions, where the RHS is positive instantaneously, i.e., where small scale vortices are created due to diffusion, represented by the first term in the RHS of Eq. (13). In Fig. 8, regions of computed RHS of the ETE (frame b) are compared with the analytical values obtained from the equilibrium solution (frame a). It is evident that the analytical RHS is negative everywhere, while one notices regions of positive RHS for the computed solution, which are first located at and around the line of symmetry of the four vortices. The instability of the disturbance enstrophy is analyzed using the theory based on the enstrophy transport equation introduced earlier.⁴¹ The linear and the non-linear growth rates of the disturbance enstrophy are evaluated, which show that the disturbance enstrophy can be either positive or negative, as it is given as $\Omega_d = \vec{\omega}_d \cdot \vec{\omega}_m$. The regions of instability are indicated by the two possibilities. The first is when $D\Omega_d/Dt > 0$ for $\Omega_d > 0$ and that shows instability. Second, when $D\Omega_d/Dt < 0$ for $\Omega_d < 0$, this also implies that the magnitude of Ω_d increases with time. The present investigation also shows the non-linear instability of the Navier-Stokes equation for the time-dependent base flow solution. While this study is novel, we intend to extend it to the full 3D Navier-Stokes equation, with the stretching term providing additional sources of disturbances as a trigger for instability.

¹G. I. Taylor and A. E. Green, "Mechanism of the production of small eddies from large ones," *Proc. R. Soc. A* **158**, 499–521 (1937).

²S. Goldstein, "Three-dimensional vortex motion in a viscous fluid," *London, Edinburgh, Dublin Philos. Mag. J. Sci.* **30**, 85–102 (1940).

³T. Gau and Y. Hattori, "Modal and non-modal stability of two-dimensional Taylor-Green vortices," *Fluid Dyn. Res.* **46**, 031410 (2014).

⁴T. K. Sengupta, *High Accuracy Computing Methods: Fluid Flows and Wave Phenomena* (Cambridge University Press, Cambridge UK, 2013).

⁵S. A. Orszag, "Numerical simulation of the Taylor-Green vortex," in *Computing Methods in Applied Sciences and Engineering Part 2: International Symposium, Versailles* (Springer Berlin Heidelberg, 1974), pp. 50–64.

⁶T. K. Sengupta, A. Sengupta, and K. Saurabh, "Global spectral analysis of multi-level time integration schemes: Numerical properties for error analysis," *Appl. Math. Comput.* **304**, 41–57 (2017).

⁷T. K. Sengupta, P. Sagaut, A. Sengupta, and K. Saurabh, "Global spectral analysis of three-time level integration schemes: Focusing phenomenon," *Comput. Fluids* **157**, 182–195 (2017).

⁸M. E. Brachet, "Direct simulation of three-dimensional turbulence in the Taylor-Green vortex," *Fluid Dyn. Res.* **8**, 1–8 (1991).

⁹M. E. Brachet, D. I. Meiron, S. A. Orszag, B. G. Nickel, R. H. Morf, and U. Frisch, "Small-scale structure of the Taylor-Green vortex," *J. Fluid Mech.* **130**, 411–452 (1983).

¹⁰M. E. Brachet, M. Meneguzzi, A. Vincent, H. Politano, and P. L. Sulem, "Numerical evidence of smooth self-similar dynamics and possibility of subsequent collapse for three-dimensional ideal flows," *Phys. Fluids A* **4**, 2845–2854 (1992).

¹¹J. DeBonis, "Solutions of the Taylor-Green vortex problem using high-resolution explicit finite difference methods," AIAA Paper 2013-0382, 2013.

¹²D. Drikakis, C. Fureby, F. F. Grinstein, and D. Youngs, "Simulation of transition and turbulence decay in the Taylor-Green vortex," *J. Turbul.* **8**, N20 (2007).

¹³C. W. Shu, W. S. Don, D. Gottlieb, O. Schilling, and L. Jameson, "Numerical convergence study of nearly incompressible, inviscid Taylor-Green vortex flow," *J. Sci. Comput.* **24**, 1–27 (2005).

¹⁴W. M. van Rees, A. Leonard, D. I. Pullin, and P. Koumoutsakos, "A comparison of vortex and pseudo-spectral methods for the simulation of periodic vortical flows at high Reynolds numbers," *J. Comput. Phys.* **230**, 2794–2805 (2011).

¹⁵G. J. Gassner and A. D. Beck, "On the accuracy of high-order discretizations for underresolved turbulence simulations," *Theor. Comput. Fluid Dyn.* **27**, 221–237 (2013).

¹⁶J. B. Chapelier, M. De La Llave Plata, and F. Renac, "Inviscid and viscous simulations of the Taylor-Green vortex flow using a modal discontinuous Galerkin approach," AIAA Paper 2012-3073, 2012.

¹⁷M. E. Brachet, M. Meneguzzi, H. Politano, and P. L. Sulem, "The dynamics of freely decaying two-dimensional turbulence," *J. Fluid Mech.* **194**, 333–349 (1988).

¹⁸P. G. Saffman, "On the boundary condition at the surface of a porous medium," *Stud. Appl. Math.* **50**, 93–101 (1971).

¹⁹R. H. Kraichnan, "Inertial ranges in two-dimensional turbulence," *Phys. Fluids* **10**, 1417–1423 (1967).

²⁰G. K. Batchelor, "Computation of the energy spectrum in homogeneous two-dimensional turbulence," *Phys. Fluids* **12**, II-233 (1969).

²¹T. K. Sengupta, S. Bhaumik, and Y. G. Bhumkar, "Direct numerical simulation of two-dimensional wall-bounded turbulent flows from receptivity stage," *Phys. Rev. E* **85**, 026308 (2012).

²²G. D. Nastrom, K. S. Gage, and W. H. Jaspersion, "Kinetic energy spectrum of large- and mesoscale atmospheric processes," *Nature* **310**, 36 (1984).

²³T. K. Sengupta and A. Sengupta, "A new alternating bi-diagonal compact scheme for non-uniform grids," *J. Comput. Phys.* **310**, 1–25 (2016).

²⁴N. Sharma, A. Sengupta, M. Rajpoot, R. J. Samuel, and T. K. Sengupta, "Hybrid sixth order spatial discretization scheme for non-uniform Cartesian grids," *Comput. Fluids* **157**, 208–231 (2017).

²⁵J. G. Charney, R. Fjörtoft, and J. von Neumann, "Numerical integration of the barotropic vorticity equation," *Tellus* **2**, 237–254 (1950).

²⁶J. Crank and P. Nicolson, "A practical method for numerical evaluation of solutions of partial differential equations of the heat-conduction type," *Math. Proc. Cambridge Philos. Soc.* **43**, 50–67 (1947).

²⁷D. W. Zingg, "Comparison of high-accuracy finite-difference methods for linear wave propagation," *SIAM J. Sci. Comput.* **22**, 476–502 (2000).

²⁸T. K. Sengupta, A. Dipankar, and P. Sagaut, "Error dynamics: Beyond von Neumann analysis," *J. Comput. Phys.* **226**, 1211–1218 (2007).

²⁹T. K. Sengupta and A. Bhole, "Error dynamics of diffusion equation: Effects of numerical diffusion and dispersive diffusion," *J. Comput. Phys.* **266**, 240–251 (2014).

³⁰V. M. Ashwin, K. Saurabh, M. Sriramkrishnan, P. M. Bagade, M. K. Parvathi, and T. K. Sengupta, "KdV equation and computations of solitons: Nonlinear error dynamics," *J. Sci. Comput.* **62**, 693–717 (2015).

³¹T. K. Sengupta, S. De, and S. Sarkar, "Vortex-induced instability of an incompressible wall-bounded shear layer," *J. Fluid Mech.* **493**, 277–286 (2003).

³²T. K. Sengupta, H. Singh, S. Bhaumik, and R. R. Chowdhury, "Diffusion in inhomogeneous flows: Unique equilibrium state in an internal flow," *Comput. Fluids* **88**, 440–451 (2013).

³³T. K. Sengupta, *Instabilities of Flows and Transition to Turbulence* (CRC Press, USA, 2012).

- ³⁴M. T. Landahl and E. Mollo-Christensen, *Turbulence and Random Processes in Fluid Mechanics* (Cambridge University Press, Cambridge, UK, 1992).
- ³⁵C. R. Doering and J. D. Gibbon, *Applied Analysis of the Navier-Stokes Equations* (Cambridge University Press, Cambridge, UK, 1995), Vol. 12.
- ³⁶H. A. Van der Vorst, "Bi-CGSTAB: A fast and smoothly converging variant of Bi-CG for the solution of nonsymmetric linear systems," *SIAM J. Sci. Stat. Comput.* **13**, 631–644 (1992).
- ³⁷M. Tobak and D. J. Peake, "Topology of three-dimensional separated flows," *Annu. Rev. Fluid Mech.* **14**, 61–85 (1982).
- ³⁸V. K. Suman, T. K. Sengupta, C. J. D. Prasad, K. S. Mohan, and D. Sanwalia, "Spectral analysis of finite difference schemes for convection diffusion equation," *Comput. Fluids* **150**, 95–114 (2017).
- ³⁹A. Sommerfeld, *Partial Differential Equation in Physics* (Academic Press, New York, 1949).
- ⁴⁰J. Weiss, "The dynamics of enstrophy transfer in two-dimensional hydrodynamics," *Phys. D* **48**, 273–294 (1991).
- ⁴¹A. Sengupta, V. K. Suman, T. K. Sengupta, and S. Bhaumik, "An enstrophy-based linear and nonlinear receptivity theory," *Phys. Fluids* (to be published).